Chemical Engineering Journal 425 (2021) 131649

Contents lists available at ScienceDirect

Chemical Engineering Journal

journal homepage: www.elsevier.com/locate/cej

Nanocatalyst-mediated oxygen depletion in epoxy coating for active corrosion protection

Meng Cheng [a], Hao Jiang [a], Zhikun Wang [a], Chunling Li [a,b], Shuangqing Sun [a,b,*], Songqing Hu [a,b,*]

[a] School of Materials Science and Engineering, China University of Petroleum (East China), Qingdao 266580, China
[b] Institute of Advanced Materials, China University of Petroleum (East China), Qingdao 266580, China

ARTICLE INFO

Keywords:
Hollow carbon spheres
Silica protected pyrolysis
Nanocatalytic anticorrosion
Smart coatings

ABSTRACT

Smart coatings depending on external nanocontainers are often complex and expensive, which can only inhibit local corrosion depending on the microenvironment change after corrosion. In this work, nanocatalytic anti-corrosion based on silica coated nitrogen enriched hollow carbon spheres (NHCs@mSiO$_2$) is developed to achieve the prolongation of coating lifetime and long-term protection of metals. Obtained NHCs@mSiO$_2$ by confined space pyrolysis strategy shows a double-shelled hollow structure with interior N-doped carbon shell and exterior silica shell. Moreover, the NHCs@mSiO$_2$ spheres possess favorable catalytic ability for oxygen thanks to the incorporation of nitrogen. When blended into epoxy coatings, amphiphilic NHCs@mSiO$_2$ spheres distribute uniformly and occupy the pores or cracks in composite coatings. The diffused oxygen through coating micropores are preferentially adsorbed by NHCs@mSiO$_2$ and directly reduced to water through four-electron pathways. Therefore, the corrosion is greatly avoided due to the depletion of oxygen. The introduction of nano-catalyst with excellent dispersity and oxygen reduction ability will pave the way toward the development of new smart coatings with active corrosion resistance.

1. Introduction

Metal products consisting of industrial equipment, bridges and vehicles are indispensable and of fundamental significance in modern industry and daily life [1,2]. However, metallic corrosion induced by aggressive working environment (water, salt, etc.), causes structural failure of metallic materials [3–5], leads to huge global loss [6,7], poses potential health risk to human beings[8–10] and has become a much-vexed issue to be addressed. Therefore, it is of great importance and significance to implement protection for corrosion-prone metals [11]. In this respect, various kinds of advanced coatings such as organic–inorganic hydride coatings [12], metallic coatings [13], and polymeric coatings [14,15], have been constantly developed to protect metals from damage.

Unfortunately, because of the inherent porous property and single passive barrier function of reported coatings, corrosive solutions are readily adsorbed and infiltrated into the substrate via capillary effect through communicating pores [16–19]. This process results in surface erosion and internal metal corrosion, which ultimately decrease the service life of coating and metal structures. Even though high-performance and high-durability coatings have been widely researched and developed [20–23], when coating is not properly protected, it undergoes performance degradation and service failure [24,25]. Moreover, it is critical to avoid degradation of the rich variety of modern products and extending their lifetime. As many engineering materials cannot be frequently replaced for efficiency, operational and cost considerations [1,26]. Therefore, this represents the motivation to design smart coatings in which the corrosion itself initiates a healing response spontaneously without human intervention.

Since White et al. pioneered the idea of smart concept to spontaneously initiate damage restoration [27], substantial amount of work has been developed to achieve smart coatings. Generally, smart coatings are composed of passive coating matrix and active nanocontainers packing inhibitors or healing agents [28,29]. Through unremitting efforts, various nanocontainers such as silica [24,30–32], grapheme [33,34], and layered double hydroxides[35,36] etc., have been incorporated into physical coatings, showing improved durability and superior resistance to corrosive species. The smart effects are realized by the release of

* Corresponding author at: School of Materials Science and Engineering, China University of Petroleum (East China), Qingdao 266580, China.
E-mail addresses: sunshuanging@upc.edu.cn (S. Sun), songqinghu@upc.edu.cn (S. Hu).

https://doi.org/10.1016/j.cej.2021.131649
Received 15 March 2021; Received in revised form 13 July 2021; Accepted 29 July 2021
Available online 9 August 2021

inhibitors from doped nanocontainers. For better control release of inhibitors and execution of smart functions, stimuli-responsive nanovalves in the form of polyelectrolyte layer-by-layer shell [37], supramolecular assembly [38–40], and pore blocking [41], etc., are installed on the surface of nanocontainers. Thanks to these gatekeepers, no appreciable premature leakage of inhibitors is achieved. What's more, the gatekeepers could sense microenvironment change (e.g., pH [32,42,43], and corrosion potential [44,45]) induced by corrosion onset and respond quickly to allow on-demand release of inhibitors to heal the corrosion sites. Nevertheless, most of the installation techniques are very complex and expensive and are still at the experimental stage. Additionally, the smart and anticorrosion enhancement of current composite coatings are realized depending on the corrosion induced stimuli, which cannot fundamentally and completely prevent the occurrence of corrosion.

It is known that corrosion is a process involving corrosive media including oxygen, water, etc. In theory, the occurrence of corrosion can be greatly reduced if the contact between oxygen and metal is well controlled [46]. Current research on oxygen reduction reaction catalyzed by nanomaterials just gives us an novel idea to solve the metal corrosion problems, inspired by the corrosion process and oxygen reduction reaction [47,48]. Catalytic oxygen reduction process involves oxygen and intermediates adsorption, and reduction to H_2O_2 or H_2O through two- or four-electron pathway. The generated H_2O_2 by two-electron pathway possesses strong oxidability and will induce degradation of polymer coatings and loss of protective effects. Therefore, it is of great significance to develop catalyst with four-electron pathway for oxygen reduction and new coatings design. In recent years, carbon-based materials have been actively studied as efficient ORR electrocatalysts because of their low cost, high durability and definite active sites [49,50]. Moreover, electrocatalytic activity can be further improved by incorporating heteroatoms (N, S, etc.) into carbon skeleton [51]. Among the synthetic methods, the direct pyrolysis of 3D heteroatom polymers is regarded as a cost-effective and facile approach to fabricate carbon catalysts. During thermal treatment under inert atmosphere, intrinsic volatile components of polymer will be depleted and the residue will form porous carbon with electrocatalytic activity. Of course, the inherent hetero elements of polymer also remain in the network of carbon catalyst. However, the micropore-dominated structure of the polymer derived carbon and the poor control over structural evolution during carbonization seriously limit the diffusion of active species and thwart the catalytic performance. Coating a silica shell with proper thickness onto the polymer spheres will help to overcome these limitations. Compared to traditional direct pyrolysis, the confined strategy can produce a higher concentration of dispersed active sites and better control over the structure of obtained catalyst, boosting catalytic performance significantly [52,53]. Thus, reasonable design of carbon catalyst with superior catalytic capacity and coating compatibility will contribute to the reduction of diffused oxygen and promoting the protective effects of anticorrosion coatings.

Herein, we propose a novel, simple, and cheap nanocatalytic anticorrosion method. Double-shelled NHCs@mSiO_2 spheres prepared by silica shell protected pyrolysis were chosen as nano-catalyst and introduced into epoxy coatings. As-prepared NHCs@mSiO_2 spheres exhibit favourable oxygen reduction performance, and the amphiphilic nature of NHCs@mSiO_2 helps them distribute uniformly in epoxy coatings. Compared to the pure epoxy coatings, diffused oxygen in the composite coatings is depleted and superior anticorrosion properties are achieved. This kind of coatings work before metal corrosion and could effectively prolong the protection time for metals. We believe that this promising nanocatalytic anticorrosion strategy will gain more attention in the research to explore more multifunctional smart coatings.

2. Materials and methods

2.1. Materials

Tetraethyl orthosilicate (TEOS), cetyltrimethylammonium bromide (CTAB) and 2-methylimidazole were purchased from Aladdin Chemistry (Shanghai) Co., Ltd. Resorcinol, formaldehyde, ethanol, methanol, ammonia solution and $Zn(NO_3)_2{\cdot}6H_2O$ were obtained from Sinopharm. Deionized water (18 MΩ cm) was used during all experiments.

2.2. Synthesis of NHCs@mSiO_2

NHCs@mSiO_2 was prepared via silica shell protected pyrolysis using oligomeric resorcinol–formaldehyde (RF) spheres as carbon source. RF spheres were obtained through the polymerization of resorcinol (0.16 g) and formaldehyde (0.24 mL, 37 wt%), which was catalyzed by ethylenediamine (0.24 mL) in a mixture of ethanol (15 mL) and deionized water (35 mL) containing 0.12 g of CTAB. Then, 50 mg of CTAB and 0.6 mL of TEOS were introduced into the resultant RF solution for coating mesoporous silica shell (mSiO_2). After stirring for 2 h at room temperature, the core/shell structured RF@mSiO_2 nanospheres were collected by centrifugation and then washed with water and ethanol several times. Finally, the hollow nanostructure NHCs@mSiO_2 was obtained by simply heating the RF@mSiO_2 nanospheres under nitrogen atmosphere at 900 °C for 3 h.

2.3. Synthesis of zeolite imidazolate frameworks (ZIF-8) and nitrogen doped carbon (NC)

1.05 g 2-methylimidazole was firstly dissolved in 100 mL methanol under sonication. Then, it was added into another pre-formed methanol solution containing 1.84 g $Zn(NO_3)_2{\cdot}6H_2O$. After stirring at room temperature for 24 h, the solid product (ZIF-8) was collected by centrifugation, washed with methanol and vacuum dried. NC was obtained by carbonization of ZIF-8 under the same condition with NHCs@mSiO_2.

2.4. Preparation of anticorrosion composite coatings

The epoxy coatings were purchased commercially. The obtained NHCs@mSiO_2 was blended into the coatings by intensive agitation for over 30 min to get a homogeneous mixture. The concentration of NHCs@SiO_2 in composite coatings is 0.8, 1.6 and 2.4 mg mL^{-1}. Then, the mixture was deposited on mild steel by automatic coater.

2.5. Coating performance

The coating performance was studied by a Gamry electrochemical workstation (Reference 600). Specifically, coated steel as working electrode was fixed in a home-made electrolyte cell containing 3.5 wt% NaCl, saturated calomel electrode, platinum electrode as reference electrode and counter electrode, respectively. The electrochemical impedance spectra (EIS) were recorded in the frequency range from 100 kHz to 0.01 Hz at open circuit potential with a sinusoidal voltage signal of 10 mV, and fitted with Zview. Potentiodynamic polarization test was also performed. Corrosion morphology was captured by ZEISS microscope.

2.6. Characterization

The structure of as-prepared nanoparticles was characterized using the Philips PW1700 X-ray diffractometer with Cu Kα radiation (1.54 Å) operated at 40 kV and 30 mA. In order to study the morphology of as-prepared particles, scanning electron microscopy (SEM) and transmission electron microscopy (TEM) images of the nanoparticles were achieved by the JEOL JSM 7500F and JEM-2100 JEOL microscope, respectively. Pore structure and surface area were characterized using

the N_2 adsorption–desorption method (Micromeritics ASAP 2010) at 77 K. Atomic force microscope (AFM) image was obtained on a Dimension 3100, Digital Instruments, Veeco Metrology Group. XPS analyses were performed using an ESCALAB 250XI electron spectrometer (Thermo Fisher Scientific, USA) with 150 W Al Ka Xray radiation as the X-ray source for excitation. Raman spectroscopies were performed using a 50 objective and a 514.5 nm laser source (Renishaw Ltd., Gloucestershire, UK).

3. Results and discussion

3.1. Characterization of NHCs@mSiO$_2$

The NHCs@mSiO$_2$ was prepared by a confined strategy shown in Scheme 1. Compared to direct pyrolysis of polymer precursor, the pyrolysis protected by silica shell happens from the interior of polymer spheres, and a void space is generated by the intrinsic volume reduction of polymer spheres after carbonization. Fig. 1a shows the SEM image of RF, all particles exhibit a spherical shape with a size around 330 nm. The core–shell structured RF@mSiO$_2$ was formed via hydrolysis and condensation of TEOS on the interface of RF particles and bulk solution. The SEM and TEM images (Fig. S1) clearly indicate that particles have a uniform core–shell structure, with a core diameter of 300 nm and a mesoporous silica (mSiO$_2$) shell thickness of 25 nm. After the pyrolysis protected by silica shell, the internal RF particles transform into a nitrogen-doped hollow carbon shell (NHCs) from interior to exterior, forming hollow NHCs@mSiO$_2$ spheres. This is because silica shell provides a driving force pulling the polymer spheres outward at carbonization [53,54]. The NHCs@mSiO$_2$ hollow nanostructure was then characterized in detail. As shown in the SEM image (Fig. 1b), it turns out that NHCs@mSiO$_2$ exhibits uniform spherical shape with an average particle size of 300 nm. The hollow nature is evidenced by broken spheres directed by the red arrows in SEM image. Moreover, the hollow nanostructure is further confirmed by TEM image in Fig. 1c. The shell thickness is about 40 nm which is obviously larger than the mSiO$_2$ shell thickness (25 nm) of RF@mSiO$_2$, suggesting the existence of NHCs shell at the internal surface. The high-magnification TEM image (Fig. 1d) also demonstrates the double shells consisted of NHCs and mSiO$_2$. The existence of elements Si, O, C, and N in the particles (Fig. 1e-i) is testified by elemental mapping, and it should be noticed that most of the elements C and N are distributed inside the hollow spheres. The NHCs fragments in the hollow cavity of NHCs@mSiO$_2$ are expected to enhance the contact with oxygen and boost the oxygen reduction action.

Nitrogen sorption and other spectroscopies were also recorded to analyze the nanoporous structure and chemical composition of the double shelled NHCs@mSiO$_2$ hollow spheres. As shown in Fig. 2a, two distinct uptakes appear at low (0–0.03) and high (0.47–0.9) relative pressure P/P_0 in nitrogen adsorption–desorption isotherm, which can confirm the microporous structure of NHCs and the mesoporous structure of mSiO$_2$, respectively. Furthermore, the existence of a hollow cavity inside the particle is verified by the hysteresis loop of the H3 type in the P/P_0 range of 0.5–1. The BET specific surface area calculated from N_2 isotherm is 263.5 $m^2 \cdot g^{-1}$. The pore size distribution derived from desorption branch shows that two different nanopores centered at 1.26 and 2.16 nm, respectively. The Raman spectrum shows two well-defined peaks located at 1336 and 1588 cm^{-1} (Fig. 2b), assigned to typical D-band and G-band of carbon, respectively. The appearance of G-band indicates the graphitic nature of the NHCs matrix. The higher I_D/I_G value suggests that there are some defect structures in the carbon framework, which might arise from the disturbance of the mSiO$_2$ shell during carbonization. The X-ray photoelectron spectroscopy (XPS) analysis shows that the sample is composed of C, H, N, O, and Si elements. High-resolution XPS spectrum of N 1 s can be resolved into three peaks located at 401.4, 400.5, and 398.6 eV (Fig. 2c), attributed to graphitic-N, pyrrolic-N, and pyridinic-N, respectively. The element analysis reveals that the carbon content is 35 wt% (Table S1), close to the result of thermogravimetric (TG) analysis (Fig. S2). The nitrogen content in the carbon matrix was as high as 1.75 wt%. The above results clearly demonstrate that the double shelled NHCs@mSiO$_2$ hollow sphere is composed of microporous NHCs and mesoporous SiO$_2$.

3.2. Nanocatalytic performance

The oxygen reduction reaction (ORR) activity of double shelled NHCs@mSiO$_2$ was evaluated by rotating disk electrode and linear sweep voltammetry (LSV) measurements. As illustrated in Fig. 2d, the oxygen reduction current density increases with the disc revolution. The inset in Fig. 2d exhibits the Koutecky-Levich (K-L) plots of NHCs@mSiO$_2$, which shows excellent linearity under different potentials, suggesting that the transferred electron numbers per oxygen molecule in ORR process are almost the same. The electron transfer number (n) of NHCs@mSiO$_2$ calculated from the slope of Koutecky-Levich plots (Fig. 2d inset) is 3.8, indicating the more efficient four-electron pathway to reduce oxygen to H_2O directly during the oxygen reduction reaction process. The NHCs@mSiO$_2$ exhibits better ORR activity than carbon nanotubes (CNTs) or grapheme [55]. The superb electrocatalytic activity can be attributed to the abundant active sites of N and defect sites distributed in the porous carbon matrix. In addition, long-term stability of NHCs@mSiO$_2$ was measured after 5000 cycles in O_2-saturated 0.1 M KOH solution. NHCs@mSiO$_2$ exhibits a 16 mV loss of $E_{1/2}$ after 5000 cycles (Fig. S4c). The Tafel slope of NHCs@mSiO$_2$ obtained from the LSVs at 1600 rpm (Fig. S4b) is 57 $mV \cdot dec^{-1}$, indicating that NHCs@mSiO$_2$ possesses a faster electron transfer rate. Besides, the long-term stability test of NHCs@mSiO$_2$ was performed by i-t chronoamperometry measurement at 0.5 V (Fig. S4d). NHCs@mSiO$_2$ exhibits a current retention of 90.5% after 30000 s. Such favourable ORR performances make it possible to achieve coating's active corrosion resistance. The superior dispersibility of NHCs@mSiO$_2$ endowed by silica shell will also contribute to better anticorrosion properties. Moreover, the influence of EDA amount on the structure and ORR performance was also investigated in detail. More regular structure and improved ORR activity are achieved with the increase of EDA amount from 0.16 to 0.24 mL (Fig. S3 and S4a). When 0.32 mL EDA was added, no obvious core–shell structure is observed (Fig. S3). This may be

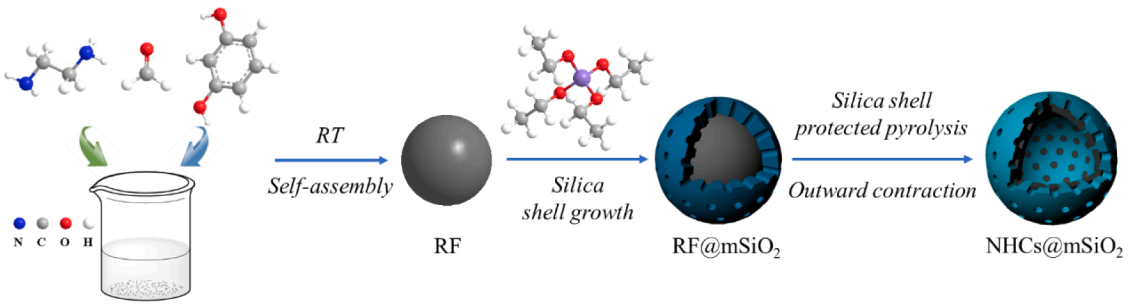

Scheme 1. Schematic illustration of the preparation for NHCs@mSiO$_2$.

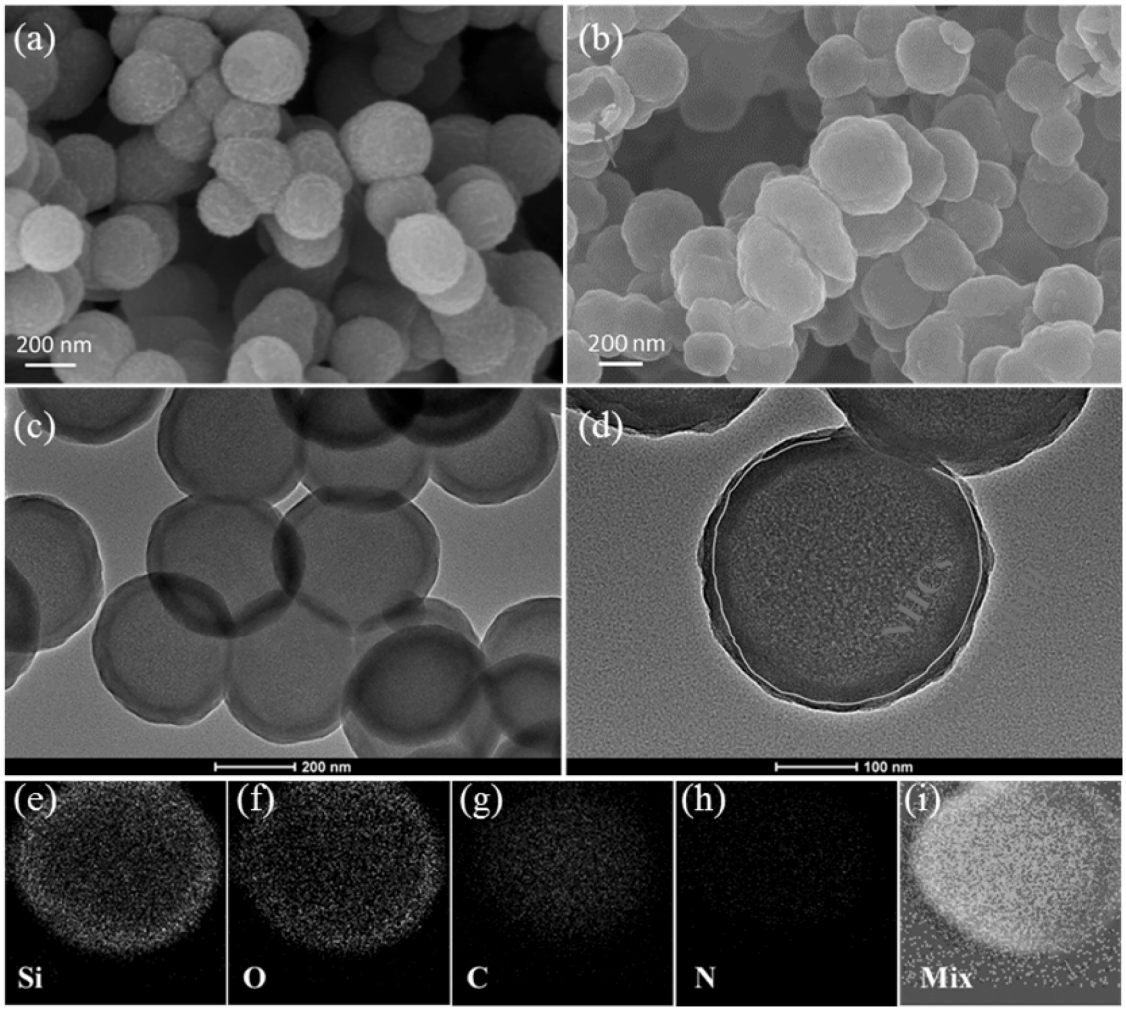

Fig 1. SEM image of RF (a). SEM image (b), TEM image (c), HETEM image (d), TEM elemental mapping images (e-i) of NHCs@mSiO$_2$.

attributed to the high polymerization degree of RF catalyzed by excessive EDA, which make it hard for the obtained RF to decompose in the silica protected pyrolysis process.

3.3. Anticorrosion performance

The high dispersibility of as-prepared NHCs@mSiO$_2$ in both aqueous and ethanolic solutions was characterized prior to its application to coating. Fig. S5 shows the uniform dispersion of NHCs@mSiO$_2$ with no agglomeration, which indicates that NHCs@mSiO$_2$ can be used in both organic and aqueous media. As shown in Fig. S5a, there is no aggregation found in the uniform dispersion of NHCs@mSiO$_2$ in epoxy-ethanol. What's more, it is pleasured that NHCs@mSiO$_2$ exhibits better dispersion in organic solvents including THF, DMF and toluene, making it promising for application in other solvent based coatings. Apart from macroscopic observation, the microscopic morphology and particle size distribution of NHCs@mSiO$_2$ are also provided (Fig. S6). It can be found that the hollow particles keep intact without apparent aggregation after dispersed in ethanol or epoxy liquid. The particle size distribution plots also demonstrate that hollow particles exhibit excellent distribution behavior, which further confirm the of result TEM. Moreover, contact angle analysis is regarded as a good way to interpret the dispersion behavior. The contact angles of NHCs@mSiO$_2$, pure epoxy coating and NHCs@mSiO$_2$ doped epoxy were recorded in Fig. S5b. NHCs@mSiO$_2$ and pure epoxy exhibit contact angles of 45° and 79°, respectively. NHCs@mSiO$_2$ doped epoxy shows slight change in contact angles (57°) compared with pure epoxy. This demonstrates that the doped NHCs@mSiO$_2$ particles are uniformly distributed inside the epoxy coating, leaving pure coating surface to bear the water droplets. All these results confirm the compatibility of NHCs@mSiO$_2$ with epoxy. There is no doubt that the doped NHCs@mSiO$_2$ will disperse uniformly in composite coating, endowing optimal performance to block corrosive species by tortuous penetration routes.

Epoxy doped with NHCs@mSiO$_2$ was coated on mild steel plates by a bar coater. The uniformity and integrality of composite coatings were revealed by the SEM characterization. No obvious aggregations are observed in both blank coating and coating with NHCs@mSiO$_2$ (Fig. S7), indicating the excellent dispersity of NHCs@mSiO$_2$ in epoxy coating matrix. Moreover, no bubbles or cracks can be found in the cross-section SEM of NHCs@mSiO$_2$ doped coating (Fig. S7c and d), which further demonstrates the structural integrity of the coating. It also can be found that NHCs@mSiO$_2$ particles are uniformly distributed in composite coatings, the bowl-like mark (red circle) is caused by the fall of NHCs@mSiO$_2$ particles during the process to obtain fractured surface by liquid nitrogen treatment. Raman spectra of the composite coating were also obtained to characterize the high uniformity and excellent dispersion of NHCs@mSiO$_2$ in the coating matrix. As mentioned previously, the corrosive species penetrate into coating through the pinhole defects. Thus, it is of great importance to achieve homogeneous distribution of NHCs@mSiO$_2$ in the coating matrix to resist permeation effect. Raman spectra recorded at five different positions are shown in Fig. 3, each spectrum at different parts of the composite coating shows identical intensity of D and G bands, indicating the homogeneous distribution of NHCs@mSiO$_2$ in coating matrix and sufficient covering for the metal

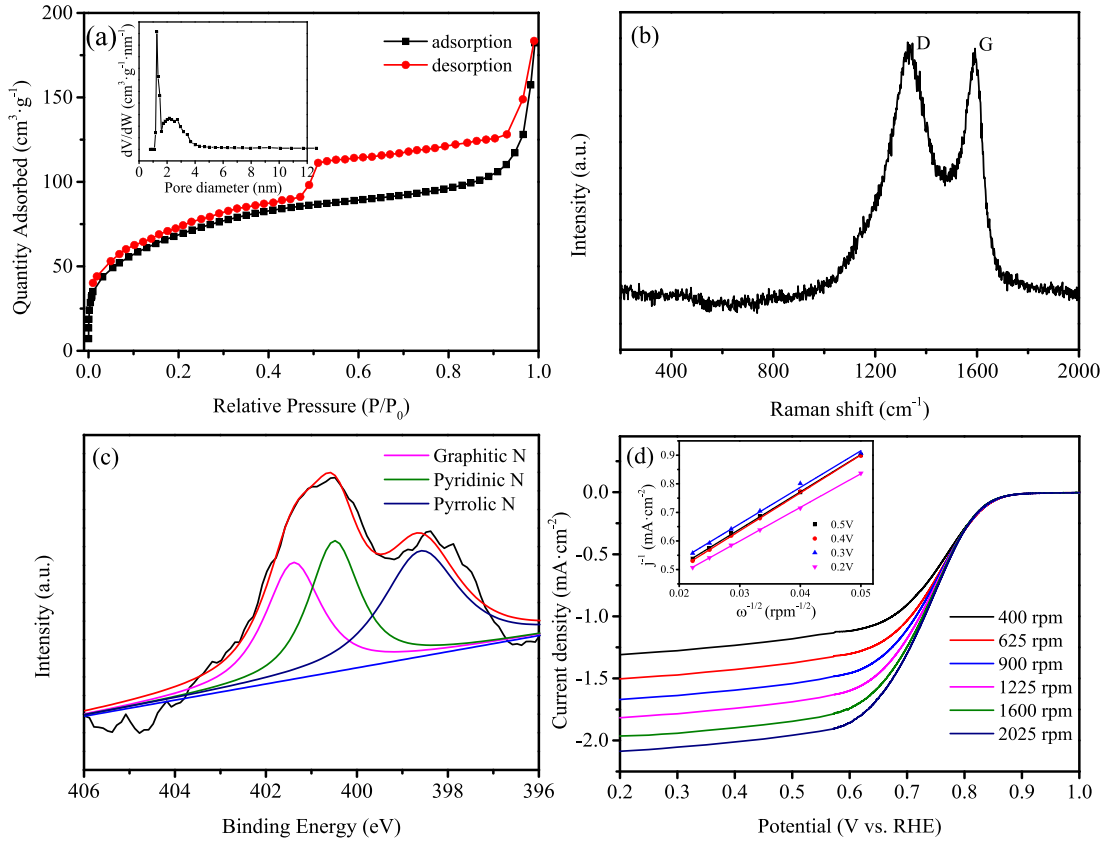

Fig 2. (a) Nitrogen adsorption–desorption isotherm (inset: pore size distribution), (b) Raman spectrum, (b) N1s XPS spectrum and (d) RDE curves with different rotation speeds (inset: K-L plots) of NHCs@mSiO$_2$.

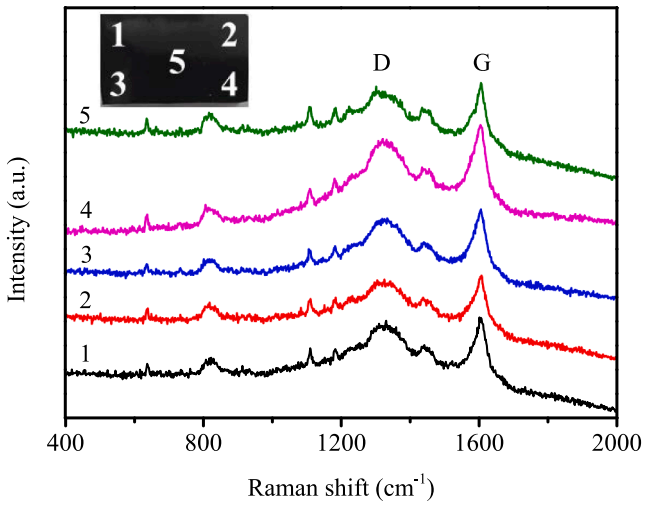

Fig 3. Raman spectra of five different positions on NHCs@mSiO$_2$ doped coating (inset: The positions on the sample where Raman spectra were recorded).

substrate at this filler content.

Electrochemical impedance spectroscopy (EIS) was performed to evaluate the corrosion properties of pure epoxy coating and coating with NHCs@mSiO$_2$ in 3.5 wt% NaCl. Fig. 4 shows the EIS spectra of experimental coatings. It can be found that the impedance value is enhanced by two orders of magnitude after addition of NHCs@mSiO$_2$ nanoparticles, both before and after the immersion test. The higher resistance suggests that the accumulation of electric charges on the mild steel coated by coating with NHCs@mSiO$_2$ is impeded. Furthermore, the resistance of NHCs@mSiO$_2$ doped coating remains nearly unchanged after 30 days of immersion, whereas the blank coating exhibits significant decrease from 1.0 × 10^4 to 0.5 × 10^4 Ω cm^2. As shown in the Nyquist plots, the capacitive loops for NHCs@mSiO$_2$ doped coating also show no appreciable change in diameter after test. In addition, two and three time constants for NHCs@mSiO$_2$ doped coating and blank coating respectively are observed after a long-term immersion of 30 days. This indicates that only slight corrosion happens under the NHCs@mSiO$_2$ doped coating whereas serious corrosion happens for steel coated by blank coating. In order to further prove the enhanced anticorrosion effect by introduced NHCs@mSiO$_2$, nitrogen doped carbon (NC) derived from direct carbonization of zeolite imidazolate frameworks (ZIF-8) is introduced into coating. Fig. S10 exhibits the microscopic morphology of NC. NC adopts dodecahedral shape and element mapping confirms the existence of carbon and nitrogen. As shown in Fig S11a, there is no obvious hysteresis loop in nitrogen sorption isotherms of NC, the pore size distribution inset further indicates that only micropores exist in NC. NC shows similar raman and XPS result with NHCs@mSiO$_2$, however, the single microporous structure does not endow NC with satisfactory ORR performance (Fig. S11d). It is no wonder that NC doped coating possesses comparable corrosion protection with blank coating (Fig. S12). It can be found that the resistance of NC doped coating decreases significantly from 1.3 × 10^6 to 4.7 × 10^4 Ω cm^2, which shows that the coating cannot provide effective long-term protective effect. In addition, the protective effect is also reflected by optical and SEM images of mild steel after removal of coatings (Fig. S13). Mild steel coated by NC doped coating exhibits serious corrosion with the corrosion pits distributing throughout the metal surface. AFM image of mild steel surface after removal of coating also show that NC doped coating does not achieve apparent improvement in corrosion protection compared

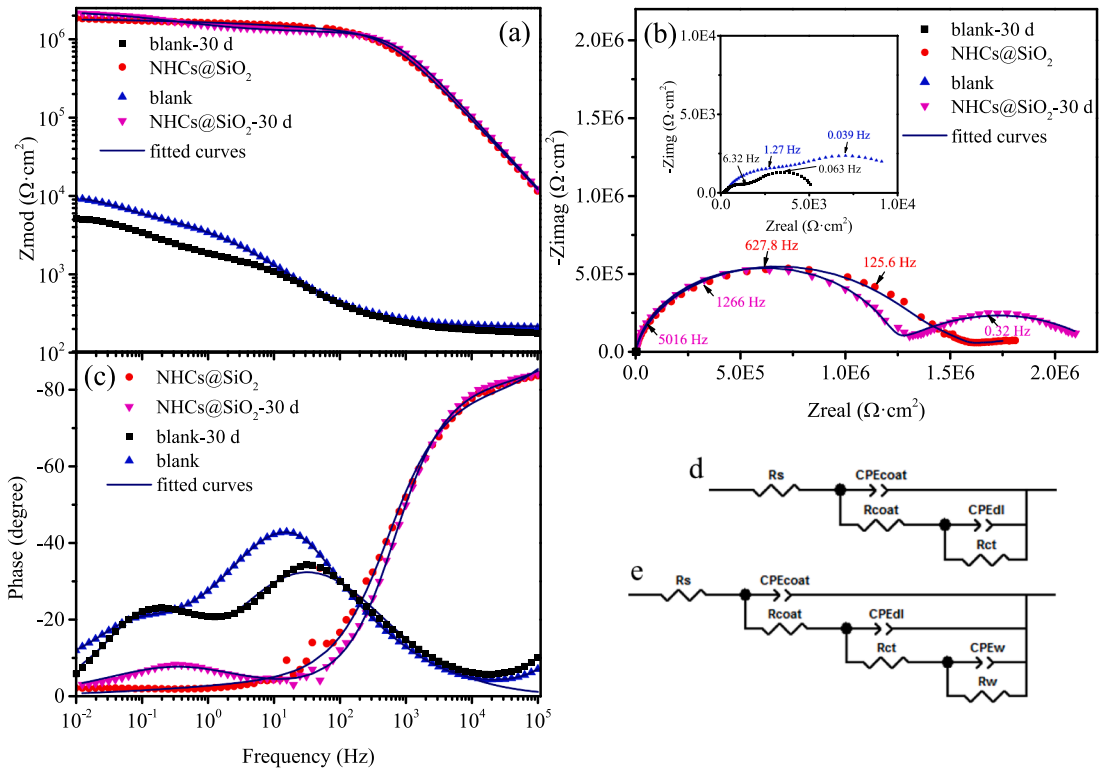

Fig 4. (a) Bode plots, (b) Nyquist plots and (c) phase angle as a function of frequency of blank coating and NHCs@mSiO$_2$ doped coating after 30 days immersion in 3.5 wt% NaCl. (d, e) Electrical equivalent circuit used for fitting EIS spectra.

with blank epoxy coating, which is consistent with the morphology characterization. All these results demonstrate that the anticorrosion performance of coating with NHCs@mSiO$_2$ nanoparticles is far superior to pure epoxy.

Next, the EIS spectra obtained after 30 days immersion in 3.5 wt% NaCl were fitted using the equivalent circuits (fit quality $\chi^2 < 0.01$) in Fig. 4d and e to deeply understand the coating electrochemical process. The solution resistance (R_s), charge transfer resistance between the mild steel and solution (R_{ct}), resistance of the coating (R_c) and Warburg impedance (W) are introduced to fully demonstrate the detailed electrochemical process of the coated samples during immersion. For better fitting results, actual electrode surface condition is considered and a

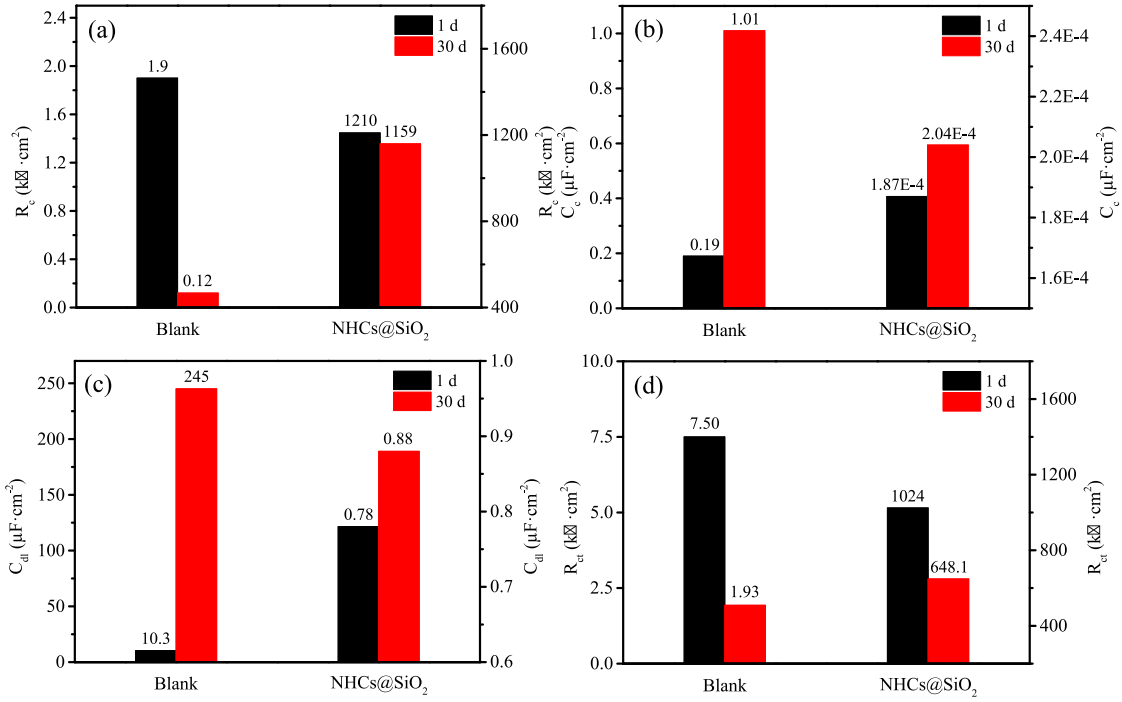

Fig 5. Variation of R_c (a), C_c (b), R_{ct} (c) and C_{dl} (d) of different coating samples after 30 days immersion in 3.5 wt% NaCl solution.

constant phase element CPE is proposed to replace C. The impedance of CPE is defined by the following equation[56,57]:

$$Z_{CPE} = Y_0^{-1}(j\omega)^{-n} \quad (1)$$

$$C = \frac{Y_0}{(\omega_{max})^{1-n}} \quad (2)$$

where Y_0 is CPE admittance, j is imaginary root, ω is angular frequency. ω_{max} is the frequency at Z_{imag} maximum. The CPE is pure capacitance when n = 1, while resistor when n = 0. The CPE is related to the morphology of electrode surface when 0 < n < 1.

As shown in Fig. 4, the experimental data well correspond to the fitting results. The detailed fitting parameters for the coating response are depicted in Table S2. Among all the parameters, R_c most directly reflects protective effect of the coating. Meanwhile, R_c is related to the coating structure and composition (pores, cracks, etc.). Thus, coating with more compact structure possesses higher R_c value and provides better protection effect. It can be found that (Fig. 5a) the R_c of coating with NHCs@mSiO$_2$ shows negligible decline compared to that of blank coating. This indicates that coating with NHCs@mSiO$_2$ always exhibits excellent and stable protective effect for coated steel, which is attributed to the effective obstruction and depletion of diffused corrosive species in composite coating by doped NHCs@mSiO$_2$. In contrast, unmodified coating is gradually degraded under the attack of corrosive species (O_2, etc.), which only serves as passive barrier without active protection function. The capacitance of coating (C_c) is another parameter reflecting coating effect. As shown in Fig. 5b, both C_c of the blank coating and coating with NHCs@mSiO$_2$ increase after immersion. By comparison, C_c of NHCs@mSiO$_2$ doped coating keeps relatively lower values and increases slightly. It has been proved that coating degradation due to gradual penetration of corrosive species induces higher coating capacitance and gradual loss of protective effect [58,59]. Accordingly, the substantial increase of higher C_c for blank coating compared to the coating with NHCs@mSiO$_2$ can explain the increasingly aggravating failure of coating effects. For lower C_c of coating with NHCs@mSiO$_2$, the pore and crack are spontaneously blocked and diffused O_2 is depleted by doped NHCs@mSiO$_2$, contributing to continuous superior protective effect. The results for both the coating capacitance and resistive response sufficiently explain the active protective effect of modified coatings from the point of specific corrosion process.

The double layer capacitance (C_{dl}) is related with the steel area exposed to electrolyte, resulting from the penetration of corrosion species through the pinhole defects in the coating. It also represents the wet adhesion of the coating to the metal substrate. Table S2 and Fig. 5c show that the value of C_{dl} for blank coating is always higher than that of coating with NHCs@mSiO$_2$, indicating a good adhesion of the coating to the steel substrate and better protective effect after immersion test. The lower C_{dl} NHCs@mSiO$_2$ doped coating is attributed to the suppression of corrosion evolution by NHCs@mSiO$_2$ with favorable oxygen reduction ability. Furthermore, R_{ct} is the most direct parameter to reflect the electrochemical process at the interface. The higher R_{ct} value with smaller decrease (Fig. 5d) of modified coating indicates that the corrosion process is effectively inhibited due to the introduction of NHCs@mSiO$_2$. Overall, active anticorrosion performance of composite coating can be achieved as corrosive species can be blocked and depleted by the doped NHCs@mSiO$_2$.

Potentiodynamic polarization was also performed to demonstrate the nanocatalytic anticorrosion effects of coating with NHCs@mSiO$_2$. The evolution of polarization curves with time is displayed in Fig. 6. The corrosion potential (E_{corr}) and corrosion current density (I_{corr}) were obtained by the Tafel fit from the linear portions of the polarization curves (Fig. S8). Specifically, the E_{corr} of pristine epoxy coating decreases from −0.78 to −1.12 V and the I_{corr} increases form 6.61×10^{-7} to 2.08×10^{-4} A·cm^{-2} (Fig. 6a) after 30 days test. In contrast, NHCs@mSiO$_2$ doped coating just shows little increase in I_{corr} from 1.94×10^{-10} to 3.11×10^{-9} A·cm^{-2} with a more positive E_{corr} of −0.51 V (Fig. 6b). It can be concluded that mild steel coated with pure epoxy is seriously corroded during 15 days. However, mild steel is well protected by NHCs@mSiO$_2$ doped coating even after immersion in 3.5 wt% NaCl solution for 30 days. This is confirmed by the more positive E_{corr} and lower I_{corr}, representing smaller corrosion probability and lower corrosion rate. These results mean that NHCs@mSiO$_2$ doped coating could maintain a less permeable barrier than epoxy for longer time because of the oxygen reduction ability of NHCs@mSiO$_2$. Therefore, corrosion is suppressed and the results are in good agreement with EIS evaluations.

Fig. 7 shows the optical images of coatings containing different concentrations of NHCs@mSiO$_2$ after immersion in 3.5 wt% NaCl solution for 30 days. For blank coating (Fig. 7a2), there are massive corrosion products appearing in the coating area, indicative of its poor corrosion resistance. In contrast, only one obvious corrosion spot is found in the local area of coating doped with NHCs@mSiO$_2$ as shown in Fig. 7b2 and d2. What's more, the coating with 1.6 mg·mL^{-1} NHCs@mSiO$_2$ shows no apparent corrosion pits. The optical and SEM images of mild steel after removal of coatings are shown in Fig. 8. It can be found that mild steel coated by blank coating exhibits the most serious corrosion, the surface pits distributed throughout the metal surface without definite pattern (Fig. 8a1-a3). In comparison, coatings with different concentrations of NHCs@mSiO$_2$ all possess better anticorrosion performance for mild steel, among which coating with 1.6 mg·mL^{-1} NHCs@mSiO$_2$ works best with no appreciable corrosion (Fig. 8b1-b3, c1-c3 and d1-d3). Overall, the diffused oxygen in coating is directly reduced to water, thus the corrosion of mild steel is inhibited, and the mass or charge transfer action at the interface of mild steel and electrolyte is terminated. The anticorrosion results are further confirmed by the tapping-mode AFM images of mild steel surface after long-term

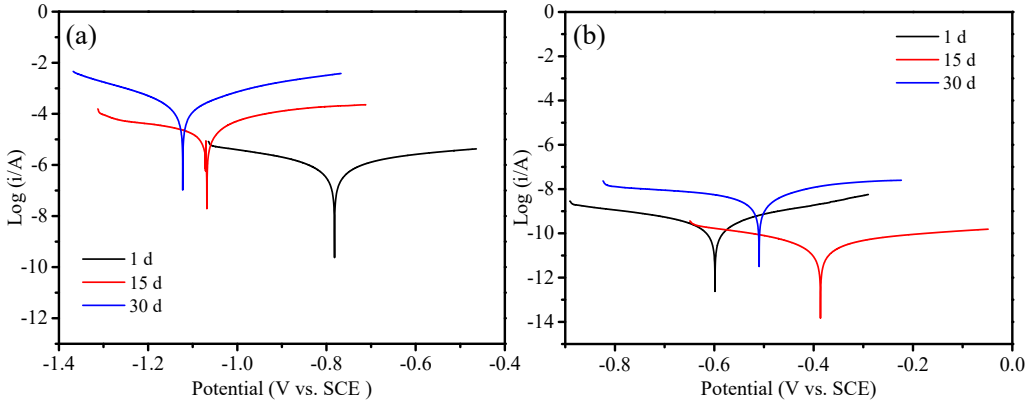

Fig 6. Polarization curves of (a) blank coating, (b) coating with NHCs@mSiO$_2$ in 3.5 wt% NaCl.

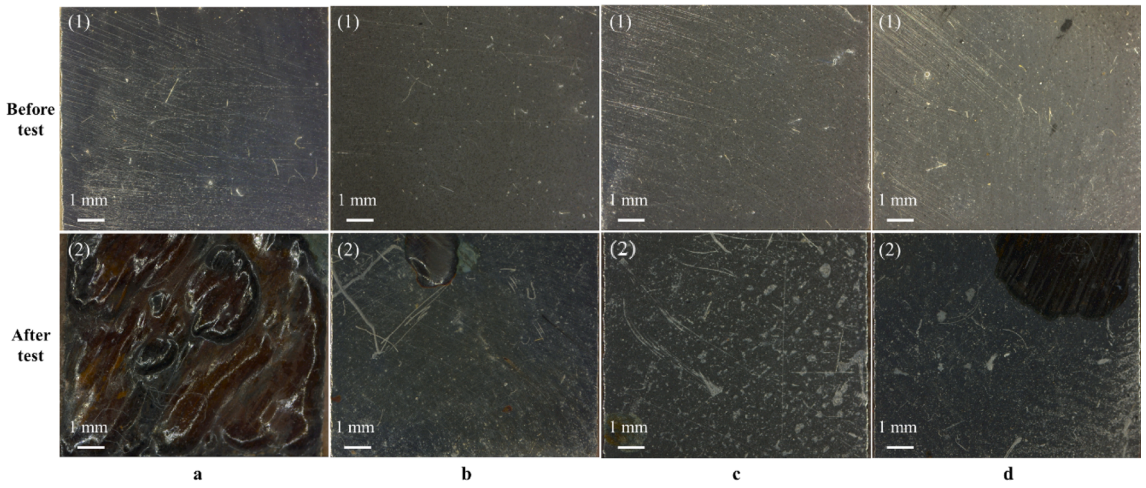

Fig 7. Optical images (a) of the blank coating and coating with (b) 0.8 mg mL^{-1}, (c) 1.6 mg mL^{-1}, and (d) 2.4 mg mL^{-1} NHCs@mSiO_2 before and after 30 days immersion.

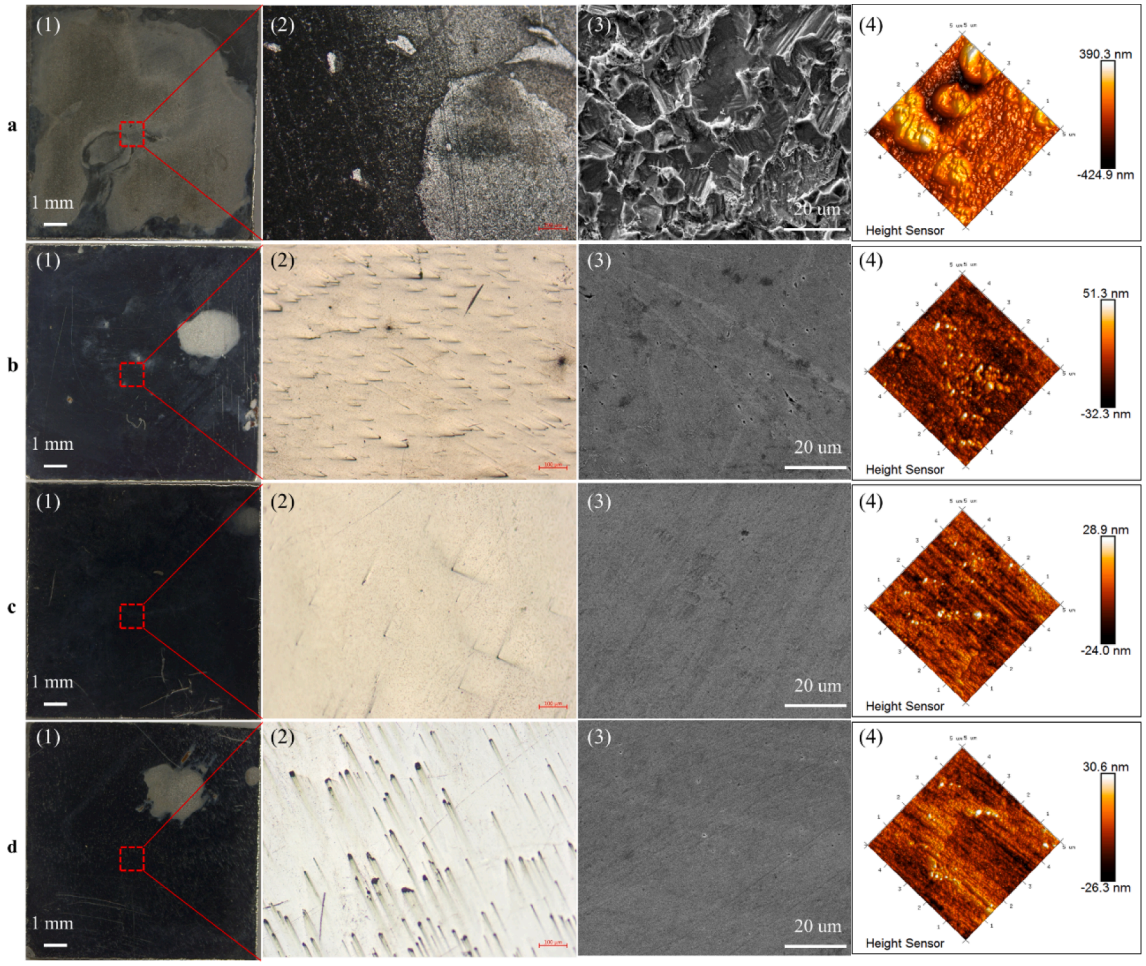

Fig 8. (a1, a2), (b1, b2), (c1, c2), (d1, d2) Optical images, (a3, b3, c3, d3) SEM images and (a4, b4, c4, d4) AFM images of steel after removal of the blank coating and coating with 0.8 mg mL^{-1}, 1.6 mg mL^{-1}, and 2.4 mg mL^{-1} NHCs@mSiO_2 after 30 days immersion.

immersion of 30 days and removal of coatings. As shown in Fig. 8a4-d4, mild steel coated blank coating shows the roughest surface with average surface roughness (φ) of 100.1 nm while mild steel protected by 1.6 mg·mL^{-1} NHCs@mSiO_2 doped coating exhibits the smoothest surface with φ of 5.4 nm. The results of AFM images are in good agreement with optical and SEM observations. Moreover, the roughness of surface at nanoscale level that is also illustrated on depth profile (Fig. S9) within the supporting information can provide supplemental explanation for the interfacial corrosion protection. For clear characterization of corrosion products, the Raman spectra of mild steel substrates were recorded after careful removal of the coatings (Fig. 9). There are three peaks attributed to γ-FeOOH and α-Fe_2O_3 appearing at 384, 590, and

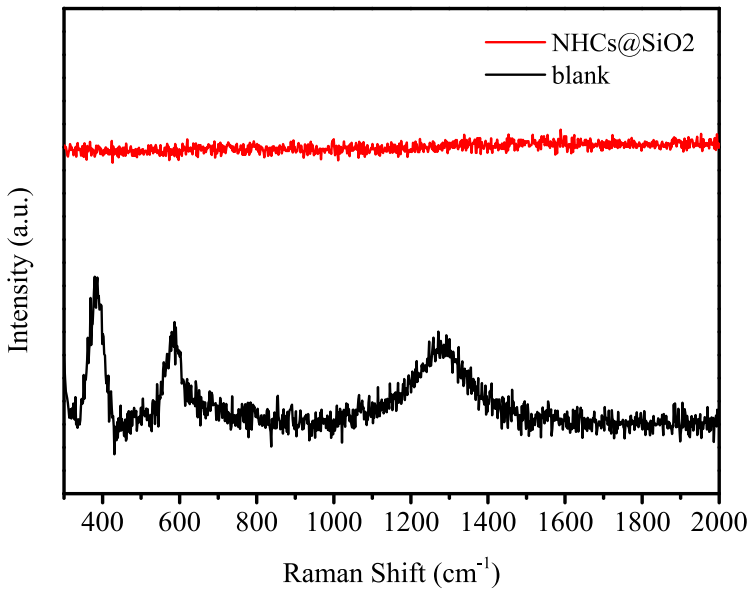

Fig 9. Raman spectra of mild steel after removal of the blank coating and coating with NHCs@mSiO$_2$ after 30 days of immersion.

1279 cm^{-1} of spectrum for the steel coated with blank coating after immersion. However, no obvious peak belongs to rust or oxide can be found from the steel coated by 1.6 mg·ml^{-1} NHCs@mSiO$_2$ doped coating, indicative its superior protection effect for the mild during immersion test. All these results prove the improved anticorrosion properties of the coating doped with NHCs@mSiO$_2$.

The protective process is described in Scheme 2 to reveal active anticorrosion mechanism of composite coating. Actually, corrosion of mild steel coated by protective coatings is induced by gradual penetration of corrosive species (e.g., O_2, H_2O, Cl^-, etc.) through the intrinsic pinhole defects of coatings. Numerous methods (e.g., smart coatings) have been developed to address this issue [28,60,61]. However, they all depend on the environment change caused by corrosion to achieve the enhancement of coating's anticorrosion performance and extension of lifetime. For composite coating in this work, it could protect metal substrates from corrosion via blocking and depletion of corrosive species (i.e. oxygen) in coatings. Specifically, the added amphiphilic NHCs@mSiO$_2$ will occupy the pores or cracks, trap oxygen and water molecules, and obstruct the crossing of them through these defects to a certain extent. Meanwhile, the catalyst nature works and the diffused oxygen is directly reduced to water through a four-electron pathway. This will slow down the corrosion rate as much as possible since the oxygen involved in corrosion process is depleted. However, such a function is not displayed in other composite coatings, which can only realize inhibition after corrosion [24,28,34].

4. Conclusions

In summary, a facile and cost-effective concept, nanocatalytic anticorrosion is proposed for the synthesis of smart composite coatings with improved active anticorrosion properties. Specifically, amphiphilic NHCs@mSiO$_2$ with favourable ORR activity distributes uniformly in composite coatings with no aggregation, which partly contributes to the suppression of intrinsic pores. Therefore, NHCs@mSiO$_2$ could effectively obstruct crossing oxygen and water through defect paths. Moreover, the hydrophilic functional groups on the surface of NHCs@mSiO$_2$ also contribute to adsorbing H_2O and trapping oxygen at the same time. Subsequently, the adsorbed O_2 molecules are directly reduced to H_2O by NHCs@mSiO$_2$ through a four-electron path. These two points endow composite coating superior active corrosion protection effect, without appreciable decrease in impedance value after 30 days of immersion in 3.5 wt% NaCl solution. Coated mild steel is well protected during this period, showing almost no corrosion. On one hand, the nanocatalytic anticorrosion initiated by the concept of introducing NHCs@mSiO$_2$ to coatings calls for a further and deeper research. On the other hand, it will open the door for designing new smart coatings and discovering their potential future applications in industry and engineering.

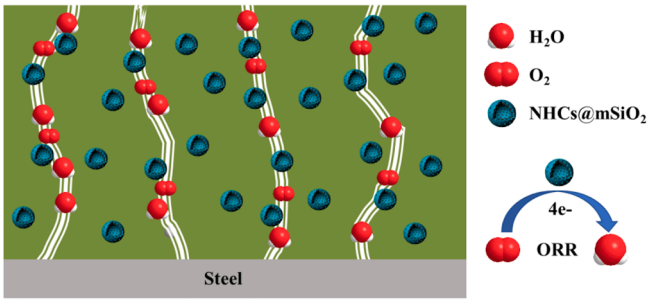

Scheme 2. Proposed active anticorrosion mechanism for coating with NHCs@mSiO$_2$ (blocking and oxygen reduction).

Declaration of Competing Interest

The authors declare that they have no known competing financial interests or personal relationships that could have appeared to influence the work reported in this paper.

Acknowledgement

This research was financially supported by the "National Natural Science Foundation of China" (51974345 and 51874331), "Shandong Provincial Natural Science Foundation, China" (ZR2019MEM054), the "Fundamental Research Funds for the Central Universities" (19CX05001A, 2019GGX102004 and YCX2020079), Project funded by China Postdoctoral Science Foundation (2020M682260) and The Applied Research Project of Qingdao Postdoctoral Researchers (qdyy20190069).

Appendix A. Supplementary data

Supplementary data to this article can be found online at https://doi.

org/10.1016/j.cej.2021.131649.

References

[1] L.L. Machuca, R. Jeffrey, S.I. Bailey, R. Gubner, E.L.J. Watkin, M.P. Ginige, A. H. Kaksonen, K. Heidersbach, Filtration–UV irradiation as an option for mitigating the risk of microbiologically influenced corrosion of subsea construction alloys in seawater, Corros. Sci. 79 (2014) 89–99.

[2] F. Suedile, F. Robert, C. Roos, M. Lebrini, Corrosion inhibition of zinc by Mansoa alliacea plant extract in sodium chloride media: extraction, characterization and electrochemical studies, Electrochim. Acta 133 (2014) 631–638.

[3] M. Tenjimbayashi, S. Nishioka, Y. Kobayashi, K. Kawase, J. Li, J. Abe, S. Shiratori, A lubricant-sandwiched coating with long-term stable anticorrosion performance, Langmuir 34 (2018) 1386–1393.

[4] X. Li, D. Zhang, Z. Liu, Z. Li, C. Du, C. Dong, Materials science: Share corrosion data, Nature News 527 (7579) (2015) 441–442.

[5] I. Díaz, H. Cano, P. Lopesino, D. de la Fuente, B. Chico, J.A. Jiménez, S.F. Medina, M. Morcillo, Five-year atmospheric corrosion of Cu, Cr and Ni weathering steels in a wide range of environments, Corros. Sci. 141 (2018) 146–157.

[6] B. Yuan, C. Bao, X. Qian, L. Song, Q. Tai, K.M. Liew, Y. Hu, Design of artificial nacre-like hybrid films as shielding to mitigate electromagnetic pollution, Carbon 75 (2014) 178–189.

[7] R.M. Erb, R. Libanori, N. Rothfuchs, A.R. Studart, Composites reinforced in three dimensions by using low magnetic fields, Science 335 (6065) (2012) 199–204.

[8] H. Zhao, Y. Yue, L. Guo, J. Wu, Y. Zhang, X. Li, S. Mao, X. Han, Cloning nacre's 3D interlocking skeleton in engineering composites to achieve exceptional mechanical properties, Adv. Mater. 28 (25) (2016) 5099–5105.

[9] S. Qiu, W. Li, W. Zheng, H. Zhao, L. Wang, Synergistic effect of polypyrrole-intercalated graphene for enhanced corrosion protection of aqueous coating in 3.5% NaCl solution, ACS Appl. Mater. Interfaces 9 (39) (2017) 34294–34304.

[10] D. Borisova, H. Möhwald, D.G. Shchukin, Influence of embedded nanocontainers on the efficiency of active anticorrosive coatings for aluminum alloys part I: influence of nanocontainer concentration, ACS Appl. Mater. Interfaces 4 (6) (2012) 2931–2939.

[11] F. Zhang, P. Ju, M. Pan, D. Zhang, Y. Huang, G. Li, X. Li, Self-healing mechanisms in smart protective coatings: a review, Corros. Sci. 144 (2018) 74–88.

[12] J. Ding, O.u. Rahman, W. Peng, H. Dou, H. Yu, A novel hydroxyl epoxy phosphate monomer enhancing the anticorrosive performance of waterborne graphene/epoxy coatings, Appl. Surf. Sci. 427 (2018) 981–991.

[13] C. Cui, A.T.O. Lim, J. Huang, A cautionary note on graphene anti-corrosion coatings, Nat. Nanotechnol. 12 (9) (2017) 834–835.

[14] X. Shi, L. Fay, Z. Yang, T.A. Nguyen, Y. Liu, Corrosion of deicers to metals in transportation infrastructure: Introduction and recent developments, Corros. Rev. 27 (2009) 23–52.

[15] M.L. Zheludkevich, J. Tedim, M.G.S. Ferreira, "Smart" coatings for active corrosion protection based on multi-functional micro and nanocontainers, Electrochim. Acta 82 (2012) 314–323.

[16] Y. González-García, S. González, R.M. Souto, Electrochemical and structural properties of a polyurethane coating on steel substrates for corrosion protection, Corros. Sci. 49 (9) (2007) 3514–3526.

[17] J. Bohannon, 'Smart coatings' research shows the virtues of superficiality, Science 309 (2005) 376–377.

[18] Z. Yu, A.T.O. Lim, S.L. Kollasch, H.D. Jang, J. Huang, Oil-Based Self-Healing Barrier Coatings: To Flow and Not to Flow, Adv. Funct. Mater. 30 (2) (2020) 1906273, https://doi.org/10.1002/adfm.201906273.

[19] D. Zang, R. Zhu, W. Zhang, X. Yu, L. Lin, X. Guo, M. Liu, L. Jiang, Corrosion-Resistant Superhydrophobic Coatings on Mg Alloy Surfaces Inspired by Lotus Seedpod, Adv. Funct. Mater. 27 (2017) 1605446.

[20] J. Baghdachi, H. Perez, P. Talapatcharoenkit, B. Wang, Design and development of self-stratifying systems as sustainable coatings, Prog. Org. Coat. 78 (2015) 464–473.

[21] E. Langer, S. Waśkiewicz, H. Kuczyńska, G. Kamińska-Bach, Self-stratifying coatings based on Schiff base epoxy resins, J. Coat. Technol. Res. 11 (6) (2014) 865–872.

[22] R. Mo, J. Hu, H. Huang, X. Sheng, X. Zhang, Tunable, self-healing and corrosion inhibiting dynamic epoxy–polyimine network built by post-crosslinking, J. Mater. Chem. A 7 (7) (2019) 3031–3038.

[23] A. Beaugendre, S. Degoutin, S. Bellayer, C. Pierlot, S. Duquesne, M. Casetta, M. Jimenez, Self-stratifying epoxy/silicone coatings, Prog. Org. Coat. 103 (2017) 101–110.

[24] J.-B. Xu, Y.-Q. Cao, L.u. Fang, J.-M. Hu, A one-step preparation of inhibitor-loaded silica nanocontainers for self-healing coatings, Corros. Sci. 140 (2018) 349–362.

[25] A. Beaugendre, S. Degoutin, S. Bellayer, C. Pierlot, S. Duquesne, M. Casetta, M. Jimenez, Self-stratifying coatings: a review, Prog. Org. Coat. 110 (2017) 210–241.

[26] C. Zhu, Y. Fu, C. Liu, Y. Liu, L. Hu, J. Liu, I. Bello, H. Li, N. Liu, S. Guo, Carbon Dots as Fillers Inducing Healing/Self-Healing and Anticorrosion Properties in Polymers, Adv. Mater. 29 (2017) 1701399.

[27] S.R. White, N.R. Sottos, P.H. Geubelle, J.S. Moore, M.R. Kessler, S.R. Sriram, E. N. Brown, S. Viswanathan, Autonomic healing of polymer composites, Nature 409 (6822) (2001) 794–797.

[28] B. Qian, Z. Zheng, M. Michailids, N. Fleck, M. Bilton, Y. Song, G. Li, D. Shchukin, Mussel-Inspired Self-Healing Coatings Based on Polydopamine-Coated Nanocontainers for Corrosion Protection, ACS Appl. Mater. Interfaces 11 (10) (2019) 10283–10291.

[29] D. Borisova, D. Akçakayıran, M. Schenderlein, H. Möhwald, D.G. Shchukin, Nanocontainer-Based Anticorrosive Coatings: Effect of the Container Size on the Self-Healing Performance, Adv. Funct. Mater. 23 (2013) 3799–3812.

[30] M.J. Hollamby, D. Fix, I. Dönch, D. Borisova, H. Möhwald, D. Shchukin, Hybrid polyester coating incorporating functionalized mesoporous carriers for the holistic protection of steel surfaces, Adv. Mater. 23 (11) (2011) 1361–1365.

[31] Z. Zheng, M. Schenderlein, X. Huang, N.J. Brownbill, F. Blanc, D. Shchukin, Influence of functionalization of nanocontainers on self-healing anticorrosive coatings, ACS Appl. Mater. Interfaces 7 (41) (2015) 22756–22766.

[32] J. Fu, T. Chen, M. Wang, N. Yang, S. Li, Y. Wang, X. Liu, Acid and alkaline dual stimuli-responsive mechanized hollow mesoporous silica nanoparticles as smart nanocontainers for intelligent anticorrosion coatings, ACS Nano 7 (12) (2013) 11397–11408.

[33] Z. Yu, L. Lv, Y. Ma, H. Di, Y. He, Covalent modification of graphene oxide by metronidazole for reinforced anti-corrosion properties of epoxy coatings, RSC Adv. 6 (22) (2016) 18217–18226.

[34] C. Liu, H. Zhao, P. Hou, B. Qian, X. Wang, C. Guo, L. Wang, Efficient Graphene/Cyclodextrin-Based Nanocontainer: Synthesis and Host-Guest Inclusion for Self-Healing Anticorrosion Application, ACS Appl. Mater. Interfaces 10 (2018) 36229–36239.

[35] E. Alibakhshi, E. Ghasemi, M. Mahdavian, B. Ramezanzadeh, A comparative study on corrosion inhibitive effect of nitrate and phosphate intercalated Zn-Al-layered double hydroxides (LDHs) nanocontainers incorporated into a hybrid silane layer and their effect on cathodic delamination of epoxy topcoat, Corros. Sci. 115 (2017) 159–174.

[36] V. Shkirskiy, P. Keil, H. Hintze-Bruening, F. Leroux, P. Vialat, G. Lefèvre, K. Ogle, P. Volovitch, Factors affecting MoO_4^{2-} inhibitor release from Zn_2Al based layered double hydroxide and their implication in protecting hot dip galvanized steel by means of organic coatings, ACS Appl. Mater. Interfaces 7 (45) (2015) 25180–25192.

[37] E.V. Skorb, D.V. Andreeva, Layer-by-Layer approaches for formation of smart self-healing materials, Polym. Chem. 4 (18) (2013) 4834, https://doi.org/10.1039/c3py00088e.

[38] G.L. Li, Z. Zheng, H. Möhwald, D.G. Shchukin, Silica/polymer double-walled hybrid nanotubes: synthesis and application as stimuli-responsive nanocontainers in self-healing coatings, ACS Nano 7 (2013) 2470–2478.

[39] Y.e. Tian, R. Guo, Y. Jiao, Y. Sun, S. Shen, Y. Wang, D. Lu, X. Jiang, W. Yang, Redox stimuli-responsive hollow mesoporous silica nanocarriers for targeted drug delivery in cancer therapy, Nanoscale Horiz. 1 (6) (2016) 480–487.

[40] J. Shen, H. Liu, C. Mu, J. Wolfram, W. Zhang, H.-C. Kim, G. Zhu, Z. Hu, L.-N. Ji, X. Liu, M. Ferrari, Z.-W. Mao, H. Shen, Multi-step encapsulation of chemotherapy and gene silencing agents in functionalized mesoporous silica nanoparticles, Nanoscale 9 (16) (2017) 5329–5341.

[41] Z. Zheng, X. Huang, M. Schenderlein, D. Borisova, R. Cao, H. Möhwald, D. Shchukin, Self-Healing and Antifouling Multifunctional Coatings Based on pH and Sulfide Ion Sensitive Nanocontainers, Adv. Funct. Mater. 23 (26) (2013) 3307–3314.

[42] C. Wang, Z. Li, D. Cao, Y.-L. Zhao, J.W. Gaines, O.A. Bozdemir, M.W. Ambrogio, M. Frasconi, Y.Y. Botros, J.I. Zink, J.F. Stoddart, Stimulated release of size-selected cargos in succession from mesoporous silica nanoparticles, Angew. Chem. Int. Ed. 51 (22) (2012) 5460–5465.

[43] C. Ding, Y. Liu, M. Wang, T. Wang, J. Fu, Self-healing, superhydrophobic coating based on mechanized silica nanoparticles for reliable protection of magnesium alloys, J. Mater. Chem. A 4 (21) (2016) 8041–8052.

[44] J. Lai, B.P. Shah, E. Garfunkel, K.-B. Lee, Versatile fluorescence resonance energy transfer-based mesoporous silica nanoparticles for real-time monitoring of drug release, ACS Nano 7 (3) (2013) 2741–2750.

[45] H. Kim, S. Kim, C. Park, H. Lee, H.J. Park, C. Kim, Glutathione-induced intracellular release of guests from mesoporous silica nanocontainers with cyclodextrin gatekeepers, Adv. Mater. 22 (38) (2010) 4280–4283.

[46] G. Tian, M. Zhang, Y. Zhao, J. Li, H. Wang, X. Zhang, H. Yan, High Corrosion Protection Performance of a Novel Nonfluorinated Biomimetic Superhydrophobic Zn-Fe Coating with Echinopsis multiplex-like Structure, ACS Appl. Mater. Interfaces 11 (41) (2019) 38205–38217.

[47] K. Yuan, D. Lutzenkirchen-Hecht, L. Li, L. Shuai, Y. Li, R. Cao, M. Qiu, X. Zhuang, M.K.H. Leung, Y. Chen, U. Scherf, Boosting Oxygen Reduction of Single Iron Active Sites via Geometric and Electronic Engineering: Nitrogen and Phosphorus Dual Coordination, J. Am. Chem. Soc. 142 (2020) 2404–2412.

[48] L. Peng, C.-T. Hung, S. Wang, X. Zhang, X. Zhu, Z. Zhao, C. Wang, Y. Tang, W. Li, D. Zhao, Versatile Nanoemulsion Assembly Approach to Synthesize Functional Mesoporous Carbon Nanospheres with Tunable Pore Sizes and Architectures, J. Am. Chem. Soc. 141 (17) (2019) 7073–7080.

[49] R. Wu, X. Wan, J. Deng, X. Huang, S. Chen, W. Ding, L.i. Li, Q. Liao, Z. Wei, NaCl protected synthesis of 3D hierarchical metal-free porous nitrogen-doped carbon catalysts for the oxygen reduction reaction in acidic electrolyte, Chem. Commun. 55 (61) (2019) 9023–9026.

[50] G. Ren, S. Chen, J. Zhang, N. Zhang, C. Jiao, H. Qiu, C. Liu, H.-L. Wang, N-doped porous carbon spheres as metal-free electrocatalyst for oxygen reduction reaction, J. Mater. Chem. A 9 (9) (2021) 5751–5758.

[51] J. Yang, F. Xiang, H. Guo, L. Wang, X. Niu, Honeycomb-like porous carbon with N and S dual-doping as metal-free catalyst for the oxygen reduction reaction, Carbon 156 (2020) 514–522.

[52] J. Du, L. Liu, Y. Yu, Y. Qin, H. Wu, A. Chen, A confined space pyrolysis strategy for controlling the structure of hollow mesoporous carbon spheres with high supercapacitor performance, Nanoscale 11 (10) (2019) 4453–4462.

[53] C. Wang, J. Kim, J. Tang, M. Kim, H. Lim, V. Malgras, J. You, Q. Xu, J. Li, Y. Yamauchi, New strategies for novel MOF-derived carbon materials based on nanoarchitectures, Chem 6 (1) (2020) 19–40.
[54] C. Liu, X. Huang, J. Wang, H. Song, Y. Yang, Y. Liu, J. Li, L. Wang, C. Yu, Hollow Mesoporous Carbon Nanocubes: Rigid-Interface-Induced Outward Contraction of Metal-Organic Frameworks, Adv. Funct. Mater. 28 (2018) 1705253.
[55] C. Zhu, Y. Fu, C. Liu, Y. Liu, L. Hu, J. Liu, I. Bello, H. Li, N. Liu, S. Guo, H. Huang, Y. Lifshitz, S.T. Lee, Z. Kang, Carbon Dots as Fillers Inducing Healing/Self-Healing and Anticorrosion Properties in Polymers, Adv. Mater. 29 (2017) 1701399.
[56] S. Ebrahimi, A. Bordbar-Khiabani, B. Yarmand, Immobilization of rGO/ZnO hybrid composites on the Zn substrate for enhanced photocatalytic activity and corrosion stability, J. Alloy. Compd. 845 (2020), 156219.
[57] A. Bordbar-Khiabani, S. Ebrahimi, B. Yarmand, In-vitro corrosion and bioactivity behavior of tailored calcium phosphate-containing zinc oxide coating prepared by plasma electrolytic oxidation, Corros. Sci. 173 (2020), 108781.
[58] D. Borisova, D. Akcakayiran, M. Schenderlein, H. Mohwald, D.G. Shchukin, Nanocontainer-Based Anticorrosive Coatings: Effect of the Container Size on the Self-Healing Performance, Adv. Funct. Mater. 23 (2013) 3799–3812.
[59] A.S. Castela, A.M. Simões, An impedance model for the estimation of water absorption in organic coatings. Part I: A linear dielectric mixture equation, Corrosion Sci. 45 (2003) 1631–1646.
[60] A. Khan, A. Hassanein, S. Habib, M. Nawaz, R.A. Shakoor, R. Kahraman, Hybrid Halloysite Nanotubes as Smart Carriers for Corrosion Protection, ACS Appl. Mater. Interfaces 12 (33) (2020) 37571–37584.
[61] M. Akhondi, E. Jamalizadeh, Fabrication of β-cyclodextrin modified halloysite nanocapsules for controlled release of corrosion inhibitors in self-healing epoxy coatings, Prog. Org. Coat. 145 (2020), 105676.